

Single E -type collinear spin state in orthorhombic $YMnO_3$


Noriki Terada^{1,*}, Tomohito Nakano,² Claire V. Colin,³ Anne Stunault,⁴ Navid Qureshi,⁴
Bachir Ouladdiaf,⁴ and Hirohiko Sato^{2,†}

¹National Institute for Materials Science, Sengen 1-2-1, Tsukuba, Ibaraki 305-0047, Japan

²Department of Physics, Chuo University, 1-13-27 Kasuga, Bunkyo-ku, Tokyo 112-8551, Japan

³Université Grenoble Alpes, CNRS, Institut Néel, F-38042 Grenoble, France

⁴Institut Laue–Langevin, BP 156, F-38042 Grenoble Cedex 9, France

 (Received 3 October 2021; revised 28 January 2022; accepted 23 March 2022; published 4 April 2022)

We studied the ferroelectricity and magnetic ordering of multiferroic orthorhombic perovskite $YMnO_3$ using magnetic and dielectric measurements and polarized/unpolarized neutron diffraction experiments with a single crystal. The ferroelectric polarization of a relatively large value $P \simeq 0.55 \mu\text{C}/\text{cm}^2$ was observed below $T = 29$ K. The magnetic \mathbf{k} vector was identified as $\mathbf{k} = (0, 0.487, 0)$ in the low-temperature ferroelectric phase. Based on the spherical neutron polarimetry experiment, the magnetic structure was determined to be of collinear E -type ordering with spins along the b axis. The E -type state did not coexist with other states in the low-temperature ferroelectric phase. A simple domain structure model indicated that a single collinear E -type structure with a small incommensurability can be realized as the magnetic ground state of $YMnO_3$.

DOI: [10.1103/PhysRevB.105.144403](https://doi.org/10.1103/PhysRevB.105.144403)

I. INTRODUCTION

Magnetoelectric (ME) multiferroic compounds with magnetic and ferroelectric orderings, have been intensively studied for the last 15 years [1,2]. In particular, cross-coupling between the spin and the ferroelectric ordering in orthorhombic perovskite manganites $RMnO_3$ (where R = rare earth or Y) has been extensively studied from both experimental and theoretical points of view [3–7]. The compounds of the $RMnO_3$ family exhibit various types of magnetic ordering with a common centrosymmetric crystal structure ($Pbnm$), and thus they provide many opportunities to study the cross-coupling phenomena. $RMnO_3$ multiferroics can be classified into two classes with different cross-coupling mechanisms. $RMnO_3$ with $R = \text{Tb}$ and Dy have an incommensurate noncollinear cycloid spin ordering, resulting in ferroelectric polarization through the inverse Dzyaloshinskii-Moriya (DM) effect, $P \propto \sum S_i \times S_j$ [3,4]. Collinear E -type magnetic ordering has been observed in $RMnO_3$ with $R = \text{Y}$, Ho , Er , Tm , Yb , and Lu [8–15]; the high-pressure phase of $R = \text{Tb}$ and Dy [16–20] also induces ferroelectricity owing to the exchange striction mechanism expressed by $P \propto \sum S_i \cdot S_j$ [5,21].

The ionic radius of Y is near the phase boundary between the cycloid and E -type collinear phases in the magnetic phase diagram of orthorhombic $RMnO_3$ [6]. Orthorhombic $YMnO_3$ (o - $YMnO_3$) exhibits successive magnetic phase transitions at $T = 42$ K and $T = 30$ K [10,13]. In previous powder neutron diffraction experiments, the magnetic propagation vector was reported to be incommensurate, $\mathbf{k} = (0, 0.435, 0)$, and the collinear spin density wave (SDW) ordering with spins

parallel to the b axis remains even at 1.7 K [10]. Moreover, the temperature dependence of the ferroelectric polarization showed a double-peak behavior below $T = 30$ K, and the polarization reached $P = 0.22 \mu\text{C}/\text{cm}^2$ at the lowest temperature in a previous single-crystal study [22]. The double-peak behavior and the small value of polarization compared to the theoretical prediction based on the exchange striction effect were attributed to the phase coexistence between the E -type and bc -cycloid phases [22]. By contrast, a large polarization value of $P = 0.7 \mu\text{C}/\text{cm}^2$ induced by the E -type ordering was observed in o - $YMnO_3$ thin films [23]. However, resonant x-ray diffraction with a thin film subsequently revealed the phase coexistence of the E -type collinear ($S||b$) and the cycloid orders ($S||bc$) [24]. Although significant effort has been devoted to studying the properties of o - $YMnO_3$ described earlier, its true magnetic ground state has not been fully understood because of the lack of neutron diffraction experiments on a single crystal.

In the present paper, first, a single crystal of o - $YMnO_3$ was grown by a hydrothermal synthesis method. Then, a detailed single-crystal analysis of the magnetic ground state was performed based on magnetization, dielectric permittivity, and pyroelectric current measurements and unpolarized/polarized neutron diffraction experiments.

II. EXPERIMENTAL DETAILS

Single crystals of o - $YMnO_3$ were grown using a hydrothermal method. In this process, the starting materials, MnO_2 , Y_2O_3 , and MgO , were sealed in a silver capsule with a small amount of KOH . This mixture was maintained at 650 °C and 150 MPa for 2 days. After the reaction, plates with an average thickness of 0.2 mm were obtained, as shown in Fig. 1(a). X-ray diffraction experiments confirmed that the

*TERADA.Noriki@nims.go.jp

†hirohiko@phys.chuo-u.ac.jp

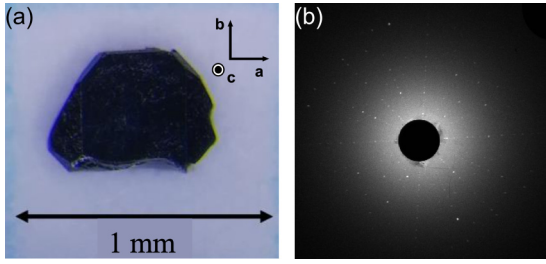


FIG. 1. (a) Photograph of the *o*-YMnO₃ single crystal. The large surface is perpendicular to the orthorhombic *c* axis. (b) X-ray Laue image taken by an x-ray beam perpendicular to the *c* axis.

crystals were single crystals. An x-ray Laue image, for which the orthorhombic *c* axis is parallel to the incoming beam, is shown in Fig. 1(b). Based on magnetization measurements on a single crystal it was confirmed within experimental accuracy that there were no magnetic impurities. In all measurements, including magnetization, dielectric permittivity, pyroelectric current, and neutron diffraction experiments, one identical sample was used.

The magnetization was measured using a magnetic property measurement system (Quantum Design, MPMS-XL). The dielectric permittivity and pyroelectric current measurements were performed using a physical property measurement system (Quantum Design, PPMS) and their values were measured using an LCR meter (Agilent, E4980A) and an electrometer (Keithley, 6517B), respectively. The electrodes were made with silver paste onto the opposite faces perpendicular to the *a* axis of the sample. For the dielectric permittivity measurement, a frequency of 100 kHz was employed. During the pyroelectric current measurements, the sample was first cooled under a poling electric field from -250 to 313 kV/m, and the pyroelectric current was measured during heating in a zero electric field. The dielectric polarization was calculated by integrating the current with respect to time. We confirmed that the sign of the dielectric polarization was reversed with the reversal of the poling electric field.

For the unpolarized neutron diffraction experiment, we used the neutron Laue diffractometer Cyclops [25] at the Institut Laue–Langevin (ILL) in Grenoble, France. A single-crystal sample with dimensions of $0.8 \times 0.4 \times 0.2$ mm³ was mounted on a standard liquid He orange cryostat, with the *a* axis approximately vertical. For the data analysis, the ES-MERALDA software was used [26].

For the spherical neutron polarimetry (SNP) experiment, we used the cryogenic polarization analysis device (CRY-OPAD) [27,28] on the IN20 beamline at the ILL [29]. The sample was identical to that used in the bulk measurements and the Cyclops experiment; an incident wavelength of 1.53 Å was employed. To determine the difference in the spin projections perpendicular to the scattering vector \mathbf{Q} for the collinear *E*-type ($\mathbf{S} \parallel \mathbf{b}$) and noncollinear structures, the scattering plane (H, K, H) was chosen for the SNP experiments. The relationship between the crystal lattice orientation and the neutron spin polarization axes in the (H, K, H) plane for the SNP experiment is shown in Fig. 2(a). Although the SNP analysis is very sensitive to the spin tilting toward the out of scattering

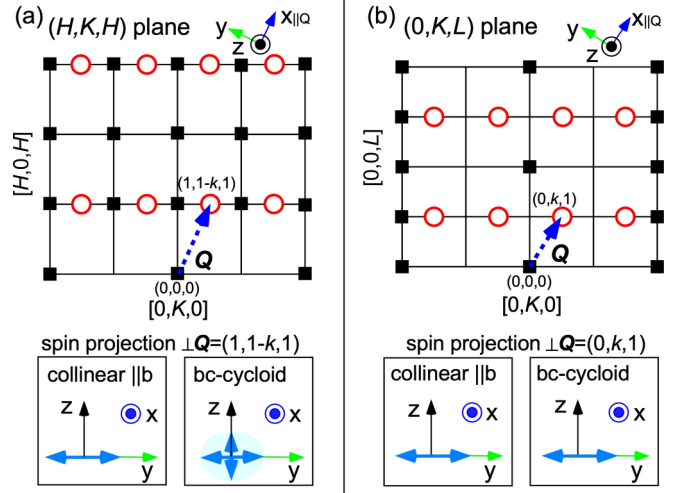


FIG. 2. Upper panels: Schematic drawings of the reciprocal lattice (a) (H, K, H) and (b) ($0, K, L$) planes in the spherical neutron polarimetry experiments. The *x*, *y*, and *z* axes denote the directions of the neutron polarization axis. The square and circle dots indicate the positions of the nuclear reflections allowed in the *Pbnm* space group, and the magnetic reflections expected from $\mathbf{k} = (0, k, 0)$, respectively. Lower panels: Relationship between spin projections perpendicular to \mathbf{Q} and neutron polarization directions for the experimental setups with (a) (H, K, H) and (b) ($0, K, L$) scattering planes. The spin projections (light blue thick arrows) of the collinear structure with spins along the *b* axis and the *bc*-cycloid structure are distinguishable for $\mathbf{Q} = (1, 1, 1) - (0, k, 0)$ in the (H, K, H) plane; they are the same for $\mathbf{Q} = (0, 0, 1) + (0, k, 0)$ in the ($0, K, L$) plane.

plane direction [30], several similar magnetic structures were not distinguishable for a highly symmetric scattering plane. For example, as shown in Fig. 2(b), the collinear structure with spins along the *b* axis and the *bc*-cycloid structure give the same result for the case of the ($0, K, L$) plane including the strongest $0, k, 1$ magnetic reflection; however, these spin models were distinguishable in the (H, K, H) plane. The polarization matrices in the SNP analysis were calculated using the MAG2POL program [30].

III. RESULTS

A. Bulk magnetic and dielectric measurements

The temperature dependence of the magnetization parallel to the orthorhombic *a*, *b*, and *c* axes is shown in Fig. 3(a). The three magnetization curves show a peak anomaly at $T = 42$ K ($\equiv T_{N1}$) without thermal hysteresis, which corresponds to the second-order phase transition from the paramagnetic (PM) phase to the SDW phase. The derivative of the magnetization as a function of temperature, dM/dT , is shown in the inset of Fig. 3(a). The dM/dT crosses zero value at T_{N1} , corresponding to the peak anomaly. A lower-temperature phase transition was detected with steep changes in the magnetization at $T = 29$ K ($\equiv T_{N2}^{\text{heat}}$) and at $T = 22$ K ($\equiv T_{N2}^{\text{cool}}$) upon heating and cooling, respectively, which is proved by observation of a peak anomaly in the temperature dependence of dM/dT at T_{N2}^{heat} and T_{N2}^{cool} [the inset of Fig. 3(a)]. The T_{N2}^{heat} value was

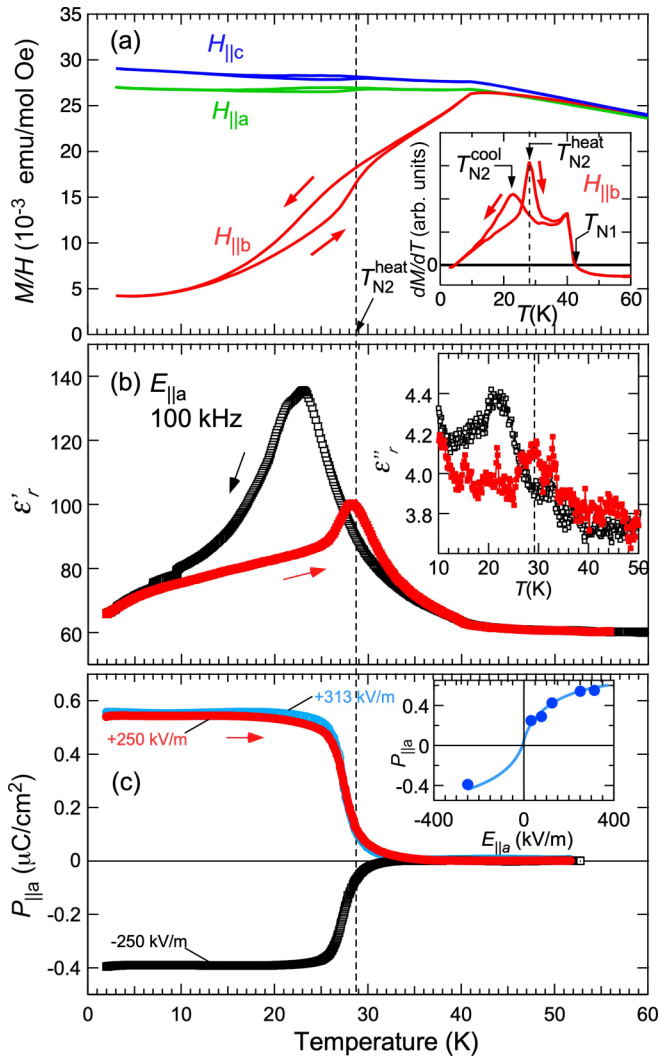


FIG. 3. Temperature dependence of (a) magnetic susceptibilities measured with magnetic fields parallel to each crystal direction, (b) real part of the dielectric permittivity, and (c) ferroelectric polarization. The inset in (a) shows the temperature dependence of the derivative of magnetization along the b axis as a function of temperature dM/dT . The inset in (b) shows the temperature dependence of the imaginary part of the dielectric permittivity. The inset in (c) shows the dependence of the ferroelectric polarization on the poling electric field.

in agreement with that in a previous report [22]. The thermal history dependence can be attributed to the first-order phase transition.

As shown in Fig. 3(b), the temperature dependence of the real part of the relative dielectric permittivity ϵ'_r along the a axis starts to rise at $T_{N1} = 42$ K with a decrease in temperature, which is independent of the temperature history. The magnetization results also indicate that the peak anomalies in ϵ'_r corresponding to the lower phase transition exhibit a significant thermal hysteresis. The peak appears at $T_{N2}^{heat} = 29$ K upon heating and $T_{N2}^{cool} = 22$ K upon cooling, which is consistent with the magnetization data. The imaginary part of the dielectric permittivity ϵ''_r [inset of Fig. 3(b)] corresponding

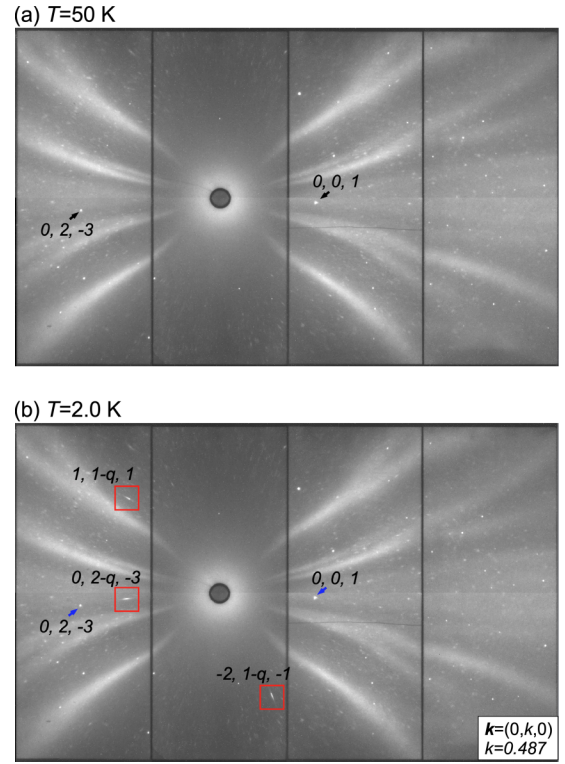


FIG. 4. Neutron Laue images at (a) 50.0 and (b) 2.0 K. The arrows and squares indicate the nuclear and magnetic reflection positions, respectively.

to the energy dissipation, also has a peak at $T_{N2}^{heat} = 29$ K and $T_{N2}^{cool} = 22$ K, which can be attributed to the ferroelectric phase transition. In the pyrocurrent measurements, we observed electric polarization along the a axis below $T = 29$ K upon heating. However, instead of the double-step behavior reported in a previous study [22] we only observed a single-phase transition. The polarization value reached $P_a = 0.55 \mu\text{C}/\text{cm}^2$, which is comparable to that observed for a thin film [23].

B. Neutron diffraction experiments

1. Magnetic propagation vector and correlation length

To study the extent of the incommensurability of the magnetic propagation vector \mathbf{k} , we first determined the temperature dependence of the magnetic Bragg reflections using unpolarized neutron diffraction measurements. Typical Laue images measured at $T = 50.0$ K and $T = 2.0$ K are shown in Fig. 4. Whereas sharp spots, indexed as nuclear reflections, can be seen at $T = 50$ K, additional broad spots corresponding to the magnetic reflections appear for the data measured at $T = 2.0$ K. These reflections can be indexed as $l, l - k, l, 0, 2 - k, -3$, and $-2, l - k, -l$ with $k = 0.487(1)$ at $T = 2.0$ K.

The temperature dependence of the magnetic propagation wave number k in $\mathbf{k} = (0, k, 0)$ is shown in Fig. 5(a). For heating in the range $29 \text{ K} \leq T \leq 42$ K and cooling in the range $22 \text{ K} \leq T \leq 42$ K, the value of k strongly depended on the temperature in the range 0.40–0.46. We also observed

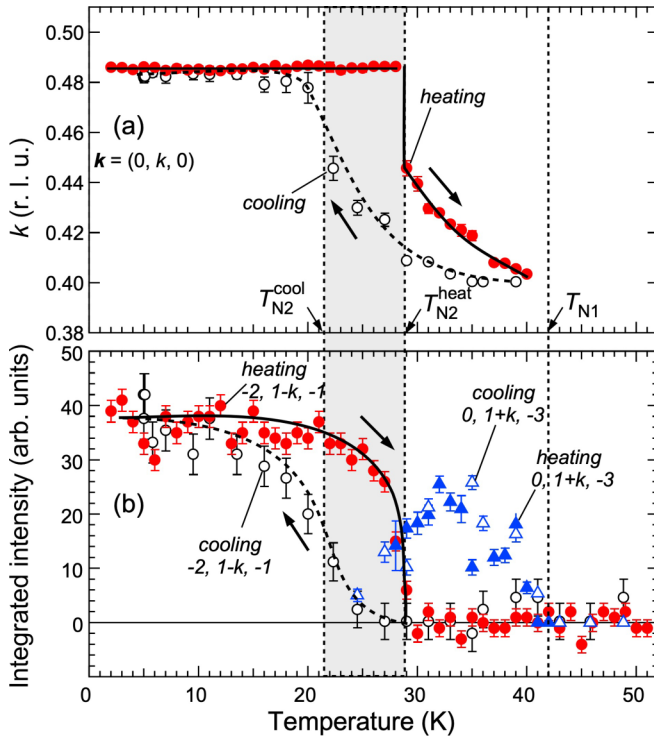


FIG. 5. Temperature dependence of (a) integrated intensity of the magnetic neutron diffraction peaks and (b) magnetic propagation wave number k of $\mathbf{k} = (0, k, 0)$. The solid and open symbols indicate the data measured during the heating and cooling processes, respectively. The temperature region where the T_{N2} shows thermal hysteresis is illustrated by shadow. These data were measured using the Cyclops diffractometer.

a large thermal hysteresis in the temperature dependence of the k vector above $T \sim 22$ K. This result suggests that the magnetic state above ~ 23 K is metastable, which includes the temperature region not only for the first-order phase transition but also in the intermediate-temperature phase with the sinusoidally modulated SDW magnetic structure. The metastable behavior in the intermediate-temperature region is similarly seen in a thermally induced state for frustrated antiferromagnetic systems [31,32].

Below $T = 29$ K for heating (or 22 K for cooling), the k value becomes a temperature-independent constant value of $k = 0.487$. Although such a temperature dependence in k was also observed in a previous powder study, the constant k value at the lowest temperature was $k = 0.435$ [10]. The temperature dependence of the integrated intensity of the magnetic Bragg reflections is shown in Fig. 5(b). Below $T = 42$ K, the intensity of the reflection with a temperature-dependent k appeared. The intensity disappeared at approximately $T = 29$ K for heating and $T = 22$ K for cooling. The intensity of the reflection with the constant value of $k = 0.487$ appeared below T_{N2}^{heat} , which was related to the appearance of electric polarization.

To investigate the magnetic correlation of ρ -YMnO₃, we measured the temperature dependence of the neutron diffraction profile below $T = 50$ K using the triple-axis spectrometer IN20. The peak positions corresponding to the

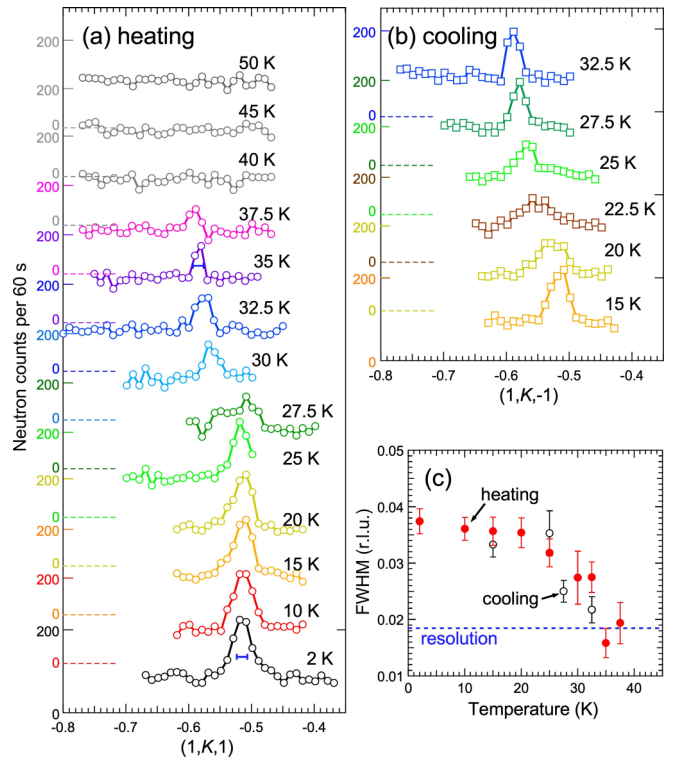


FIG. 6. Temperature dependence of the neutron diffraction profile along the reciprocal lattice $[1, K, 1]$ line, measured during (a) heating and (b) cooling, respectively. (c) Temperature dependence of the full width at half maximum of the $1, -1 + k, 1$ reflection. The solid and open symbols denote the data measured during the heating and cooling processes, respectively. The experimental resolution width is represented by a dotted line. These data were measured using the IN20 triple-axis spectrometer.

k vector value are in good agreement with the data obtained using Cyclops, as shown in Figs. 6(a) and 6(b). Double-peak behaviors were observed at $T = 27.5$ K for heating and $T = 22.5$ K for cooling, which corresponded to the coexistence of the low- and intermediate-temperature phases. The linewidth and full width at half maximum (FWHM) of the magnetic peak were nearly the same as the experimental resolution width around $T = 35$ K, whereas the width increased below $T \simeq 30$ K. This indicates that the magnetic correlation lengths for the lower part of the intermediate phase and the low-temperature phase are finite. The correlation length at 2.0 K was estimated to be 190 ± 15 Å (~ 30 sites).

2. Magnetic structure

Based on the previous description of the commensurate magnetic structure in orthorhombic perovskite systems [8,14], we first discuss the symmetry considerations for the possible magnetic structures in the low-temperature [$T \leq T_{N2}^{\text{heat}}$ (T_{N2}^{cool})] and the intermediate-temperature [T_{N2}^{heat} (T_{N2}^{cool}) $\leq T \leq T_{N1}$] phases. If a commensurate order with $\mathbf{k} = (0, 0.5, 0)$ is assumed in the low-temperature ferroelectric phase, we can identify two two-dimensional irreducible representations (IRs), mX_1 and mX_2 , at the Mn(4a) site in the $Pbnm$ space

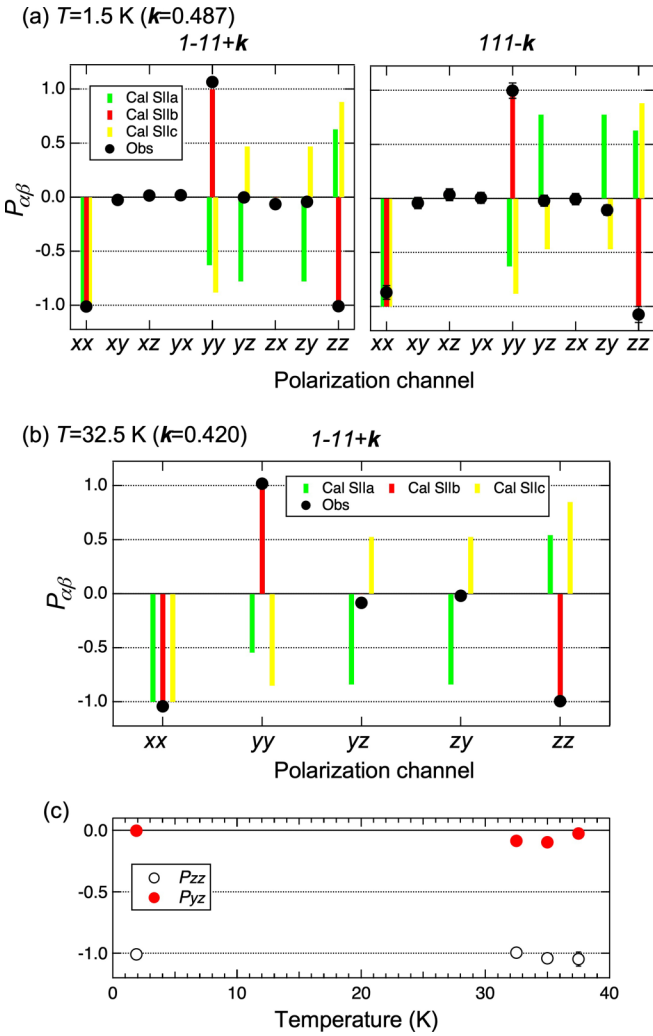


FIG. 7. Comparison of observed (circles) and calculated (bars) neutron polarization matrix elements at (a) 1.5 and (b) 32.5 K. (c) Temperature dependence of the P_{yz} and P_{zz} matrix elements. These data were measured using the CRYOPAD apparatus on the IN20 beamline.

group [34,35]. For this analysis, we selected IRs that restrict the electric polarization along the *a*-axis only. All possible magnetic symmetries for the IRs are listed in Supplemental Table I [36]. In the low-temperature phase, magnetic reflections were observed for $\mathbf{Q} = (m, n, l) \pm \mathbf{k}_{\text{Mn}}$ with $l = \text{odd}$, whereas they were not observed for $l = \text{even}$ [Fig. 4(b)], which corresponded to an antiferromagnetic arrangement along the *c* axis. These conditions restrict the magnetic moments and basis functions of the Fourier components of the magnetic moment $(m_a, m_b, 0)$ for mX_1 or $(0, 0, m_c)$ for mX_2 .

To distinguish the collinear *E*-type magnetic structure ($S||b$) from other possibilities, in the SNP experiment, the (H, K, H) scattering plane was chosen. As shown in Fig. 7(a), the possibility of the $(0, 0, m_c)$ model for mX_2 can be excluded. The experimental data are in good agreement with $(m_a, m_b, 0)$ for the mX_1 with the refined spin component ratio of $m_a/m_b = -0.014 \pm 0.015$, which corresponds to the *E*-type ordering with Mn spins parallel to the *b* axis. The

accuracy of the spin canting from the *b* axis toward the $\pm a$ axis was estimated to be $\pm 1.7^\circ$. The magnetic space group for the *E*-type ordering is polar with the P_bmn2_1 symmetry [with a basis $(0, 0, 1), (0, 2, 0), (-1, 0, 0)$], allowing a spontaneous polarization along the *a* axis in the $Pbnm$ setting.

As described in a previous study [33], the magnetic structure in the intermediate phase in orthorhombic perovskite manganites is a sinusoidally modulated SDW structure with spins along the *b* axis. In the present SNP experiment, we confirmed that the spin direction was along the *b* axis at $T = 32.5$ K; moreover, the spin direction did not change in the intermediate-temperature phase, as shown in Figs. 7(b) and 7(c).

It should be noted that the previous powder neutron diffraction study concluded that the collinear SDW structure fits the experimental result for the low-temperature data [10]. In the unpolarized neutron experiment, the SDW ordering gave fundamental magnetic neutron intensities that were the similar to those in the case of the collinear *E*-type structure, apart from higher harmonic intensities that are not included in a normal magnetic structure analysis.

IV. DISCUSSION

In this section, we discuss the origin of the small incommensurability of the *E*-type ordering in the low-temperature ferroelectric phase. In the neutron diffraction experiments in this study, the \mathbf{k} vector was proved to be slightly incommensurate with a k value (0.487) starting from 0.5. The spin direction was found to be parallel to the *b* axis without *a* and *c* components within the experimental accuracy of the SNP experiment. Unlike the intermediate-temperature phase, the sinusoidally modulated SDW ordering cannot be a solution for the low-temperature phase because of the fully polarized Mn^{3+} magnetic moments in the insulating system. In order to explain the incommensurability, we here consider the finite size of the antiferromagnetic domains formed by the *E*-type order. If the domain walls were randomly distributed due to a crystal deficiency or grain boundaries, the domain state could not make the k vector incommensurate but would just give peak broadening around the commensurate position ($k = 0.5$). On the other hand, when the domain walls are periodically distributed, the incommensurability can be explained by using a simple domain structure model. Assuming that the spin projection with a finite domain size (N), $\rightarrow \rightarrow \leftarrow \leftarrow \rightarrow \rightarrow \leftarrow \leftarrow \dots$ along the *b* axis is separated by dephased spins, $\leftarrow \leftarrow \leftarrow \rightarrow \rightarrow$, as domain walls [Fig. 8(a)], we calculated the Fourier transformation of the total spin arrangement ($|S_b(k)|$) with a system size of $N = 100$. As shown in Fig. 8(b), with the decrease in the domain size, the peak position of $|S_b(k)|$ deviates from the commensurate position $k = 0.5$. Comparing the calculated $|S_b(k)|$ to the experimental value of $k = 0.487$, we found that the domain size of $N \sim 40$ can approximately reproduce the experimental value. The expected domain size is nearly consistent with the correlation length, ~ 30 sites, estimated from the peak width of the magnetic reflection mentioned above.

However, there still remains an unsolved issue regarding why such the domain walls can be periodically distributed. In type-II multiferroics, antiferromagnetic domains are always

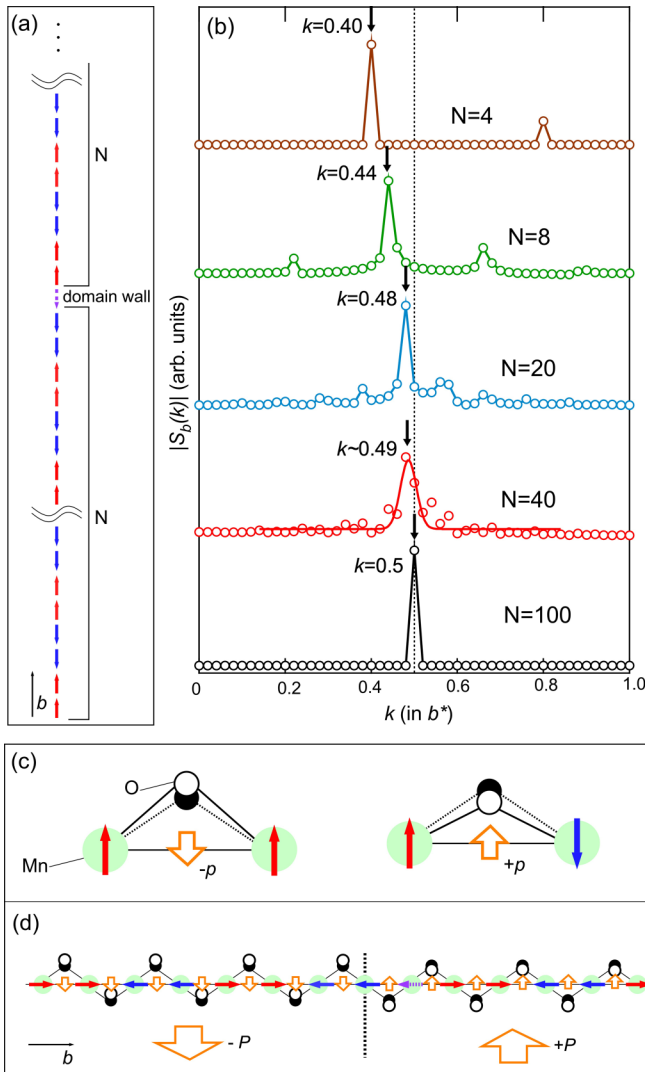


FIG. 8. (a) Schematic drawing of the magnetic domain structure for the collinear E -type magnetic structure. The thick arrows indicate the spin projection perpendicular to the b axis. The domain wall is generated by dephased spin modulation on the site represented by the dotted arrow. N is the number of projected spins in the one E -type structure domain. (b) Fourier transformations of the spin arrangement along the b axis, calculated for $N = 4, 8, 20, 40,$ and 100 . (c) Schematic drawings of oxygen displacement expected by the exchange striction mechanism for the cases of ferromagnetic and antiferromagnetic arrangements. Oxygen ions are placed at the positions represented by the solid black circles in the paramagnetic phase, while they are displaced to the positions represented by the open circles through the exchange striction in the magnetically ordered phase, which induce the local electric dipole moments $-p$ or $+p$. (d) Schematic illustration of the multiferroic domain state for E -type magnetic ordering in σ -YMnO₃. The ferroelectric domain wall generates the dephased magnetic modulation. The dotted line denotes the multiferroic domain wall.

coupled to the ferroelectric domains, which create multiferroic domains, as proved in several examples [37,38]. In σ -YMnO₃, the collinear E -type magnetic ordering induces the ferroelectric lattice displacements in each Mn-O-Mn bond,

leading to macroscopic ferroelectric polarization through the exchange striction mechanism as illustrated in Fig. 8(c) [5]. Therefore, when the ferroelectric domains are formed in the ferroelectric phase in σ -YMnO₃, the E -type antiferromagnetic order domains are simultaneously formed, as illustrated in Fig. 8(d). In general ferroelectric materials, ferroelectric domain structures formed at the paraelectric-ferroelectric phase transition are strongly dependent on the elastic boundary conditions and crystallite sizes. Although the ferroelectric (or multiferroics) domain size in σ -YMnO₃ has not been determined at the present stage, the strong sample dependence in the incommensurability between the single crystal $k = 0.487$ and the powder samples ($k = 0.435$) [10] might be caused by the difference in the ferroelectric domain formation depending on the sample conditions such as the elastic boundary conditions and grain sizes.

The measured ferroelectric polarization $P \simeq 0.55 \mu\text{C}/\text{cm}^2$ is larger than that reported in previous single-crystal ($P = 0.22 \mu\text{C}/\text{cm}^2$) [22] and powder ($P < 0.1 \mu\text{C}/\text{cm}^2$) [13] studies in σ -YMnO₃. For the single-crystal thin film, the polarization was reported to be $P \simeq 0.7 \mu\text{C}/\text{cm}^2$ [23], which is similar to the bulk single-crystal value in this study. The incommensurability of the thin film, $k \sim 0.49$, is also close to the value presented here. Therefore, we found that the ferroelectric polarization value in σ -YMnO₃ is strongly related to the incommensurability of the collinear E -type ordering. However, the thin-film x-ray study demonstrated that the c component of spin exists in the low-temperature phase of σ -YMnO₃, which can be explained by the coexistence of the bc -cycloid ordering in the E -type phase [24]. This is not consistent with the single E -type state determined in the present SNP study. This inconsistency between the bulk and thin film has not been clarified at the present stage. However, it might not be necessary that the magnetic ground state of the thin film is identical to the bulk one, because there is a difference in the lattice parameters, due to the strain from substrates in the thin film of σ -YMnO₃. In fact, for the other orthorhombic perovskite multiferroics RMnO₃ ($R = \text{Gd-Lu}$), the magnetic ground states have different magnetic structures [7].

V. CONCLUSIONS

The magnetic and dielectric properties of orthorhombic perovskite multiferroic σ -YMnO₃ were studied by bulk magnetic and dielectric measurements and unpolarized and polarized neutron diffraction experiments using a single crystal grown by a hydrothermal method. The ferroelectric polarization of the value $P \simeq 0.55 \mu\text{C}/\text{cm}^2$ was observed along the a axis below $T = 29 \text{ K}$, which was larger than that reported in previous studies [13,22]. In the neutron diffraction experiment, the magnetic \mathbf{k} vector was identified as $\mathbf{k} = (0, 0.487, 0)$ in the low-temperature ferroelectric phase. The incommensurability [deviation from the commensurate value $(0, 0.5, 0)$] in the single-crystal case in this study was significantly smaller than that of the powder sample [$\mathbf{k} = (0, 0.435, 0)$] [10]. From the SNP experiment, the magnetic structure was determined to be of collinear E -type ordering with spins along the b axis. Unlike the previous thin-film study [24], a phase coexistence between the E -type

and *bc*-cycloid states was not observed. A simple domain structure model of the collinear *E*-type structure indicated that the single collinear *E*-type structure can explain the small incommensurability observed in the ferroelectric phase of *o*-YMnO₃.

ACKNOWLEDGMENTS

We thank the ILL for providing neutron beamtime access [29]. This work was supported by JSPS KAKENHI Grants (No. 17KK0099 and No. 19H04400) and the JST-Mirai Program, Japan Grant (No. JPMJMI18A3).

- [1] T. Kimura, T. Goto, H. Shintani, K. Ishizaka, T. Arima, and Y. Tokura, *Nature (London)* **426**, 55 (2003).
- [2] S.-W. Cheong and M. Mostovoy, *Nat. Mater.* **6**, 13 (2007).
- [3] H. Katsura, N. Nagaosa, and A. V. Balatsky, *Phys. Rev. Lett.* **95**, 057205 (2005).
- [4] M. Mostovoy, *Phys. Rev. Lett.* **96**, 067601 (2006).
- [5] I. A. Sergienko, C. Sen, and E. Dagotto, *Phys. Rev. Lett.* **97**, 227204 (2006).
- [6] S. Ishiwata, Y. Kaneko, Y. Tokunaga, Y. Taguchi, T. H. Arima, and Y. Tokura, *Phys. Rev. B* **81**, 100411(R) (2010).
- [7] K. Shimamoto, S. Mukherjee, N. S. Bingham, A. K. Suszka, T. Lippert, C. Niedermayer, and C. W. Schneider, *Phys. Rev. B* **95**, 184105 (2017).
- [8] A. Muñoz, J. A. Alonso, M. T. Casáis, M. J. Martínez-Lope, J. L. Martínez, and M. T. Fernández-Díaz, *Inorg. Chem.* **40**, 1020 (2001).
- [9] H. W. Brinks, J. Rodríguez-Carvajal, H. Fjellvag, A. Kjekshus, and B. C. Hauback, *Phys. Rev. B* **63**, 094411 (2001).
- [10] A. Muñoz, J. A. Alonso, M. T. Casais, M. J. Martínez-Lope, J. L. Martínez, and M. T. Fernández-Díaz, *J. Phys.: Condens. Matter* **14**, 3285 (2002).
- [11] Y. H. Huang, H. Fjellvåg, M. Karppinen, B. C. Hauback, H. Yamauchi, and J. B. Goodenough, *Chem. Mater.* **18**, 2130 (2006).
- [12] F. Ye, B. Lorenz, Q. Huang, Y. Q. Wang, Y. Y. Sun, C. W. Chu, J. A. Fernandez-Baca, P. Dai, and H. A. Mook, *Phys. Rev. B* **76**, 060402(R) (2007).
- [13] B. Lorenz, Y.-Q. Wang, and C.-W. Chu, *Phys. Rev. B* **76**, 104405 (2007).
- [14] V. Y. Pomjakushin, M. Kenzelmann, A. Donni, A. B. Harris, T. Nakajima, S. Mitsuda, M. Tachibana, L. Keller, J. Mesot, H. Kitazawa, and E. Takayama-Muromachi, *New J. Phys.* **11**, 043019 (2009).
- [15] S. Mukherjee, A. Donni, T. Nakajima, S. Mitsuda, M. Tachibana, H. Kitazawa, V. Pomjakushin, L. Keller, C. Niedermayer, A. Scaramucci, and M. Kenzelmann, *Phys. Rev. B* **95**, 104412 (2017).
- [16] T. Aoyama, K. Yamauchi, A. Iyama, S. Picozzi, K. Shimizu, and T. Kimura, *Nat. Commun.* **5**, 4927 (2014).
- [17] T. Aoyama, A. Iyama, K. Shimizu, and T. Kimura, *Phys. Rev. B* **91**, 081107(R) (2015).
- [18] O. L. Makarova, I. Mirebeau, S. E. Kichanov, J. Rodríguez-Carvajal, and A. Forget, *Phys. Rev. B* **84**, 020408(R) (2011).
- [19] N. Terada, D. D. Khalyavin, P. Manuel, T. Osakabe, A. Kikkawa, and H. Kitazawa, *Phys. Rev. B* **93**, 081104(R) (2016).
- [20] N. Terada, N. Qureshi, A. Stunault, M. Enderle, B. Ouladdiaf, C. V. Colin, D. D. Khalyavin, P. Manuel, F. Orlandi, S. Miyahara, D. Prabhakaran, and T. Osakabe, *Phys. Rev. B* **102**, 085131 (2020).
- [21] M. Mochizuki, N. Furukawa, and N. Nagaosa, *Phys. Rev. B* **84**, 144409 (2011).
- [22] S. Ishiwata, Y. Tokunaga, Y. Taguchi, and Y. Tokura, *J. Am. Chem. Soc.* **133**, 13818 (2011).
- [23] M. Nakamura, Y. Tokunaga, M. Kawasaki, and Y. Tokura, *Appl. Phys. Lett.* **98**, 082902 (2011).
- [24] H. Wadati, J. Okamoto, M. Garganourakis, V. Scagnoli, U. Staub, Y. Yamasaki, H. Nakao, Y. Murakami, M. Mochizuki, M. Nakamura, M. Kawasaki, and Y. Tokura, *Phys. Rev. Lett.* **108**, 047203 (2012).
- [25] B. Ouladdiaf, J. Archer, J. R. Allibon, P. Decarpentrie, M.-H. Lemée-Cailleau, J. Rodríguez-Carvajal, A. W. Hewat, S. York, D. Brau, and G. J. McIntyre, *J. Appl. Cryst.* **44**, 392 (2011).
- [26] L. Fuentes-Montero, P. Cermak, J. Rodríguez-Carvajal, and A. Filhol, The *ESMERALDA* suite, doi: 10.13140/RG.2.1.4954.1202.
- [27] F. Tasset, *Phys. B: Condens. Matter* **156-157**, 627 (1989).
- [28] F. Tasset, P. J. Brown, E. Lelièvre-Berna, T. Roberts, S. Pujol, J. Allibon, and E. Bourgeat-Lami, *Physica B* **267-268**, 69 (1999).
- [29] Institut Laue-Langevin (ILL), doi: 10.5291/ILL-DATA.5-54-323
- [30] N. Qureshi, *J. Appl. Cryst.* **52**, 175 (2019).
- [31] N. Terada, T. Nakajima, S. Mitsuda, H. Kitazawa, K. Kaneko, and N. Metoki, *Phys. Rev. B* **78**, 014101 (2008).
- [32] N. Terada, D. D. Khalyavin, P. Manuel, Y. Tsujimoto, K. Knight, P. G. Radaelli, H. S. Suzuki, and H. Kitazawa, *Phys. Rev. Lett.* **109**, 097203 (2012).
- [33] M. Kenzelmann, A. B. Harris, S. Jonas, C. Broholm, J. Schefer, S. B. Kim, C. L. Zhang, S.-W. Cheong, O. P. Vajk, and J. W. Lynn, *Phys. Rev. Lett.* **95**, 087206 (2005).
- [34] B. J. Campbell, H. T. Stokes, D. E. Tanner, and D. M. Hatch, *J. Appl. Cryst.* **39**, 607 (2006).
- [35] J. M. Perez-Mato, J. L. Ribeiro, V. Petricek, and M. I. Aroyo, *J. Phys.: Condens. Matter* **24**, 163201 (2012).
- [36] See Supplemental Material at <http://link.aps.org/supplemental/10.1103/PhysRevB.105.144403> for a list of magnetic distortion modes of two possible irreducible representations for the little group of *Pbnm* with $k = (0, 1/2, 0)$.
- [37] T. Hoffmann, P. Thielen, P. Becker, L. Bohaty, and M. Fiebig, *Phys. Rev. B* **84**, 184404 (2011).
- [38] P. Schoenherr, S. Manz, L. Kuerten, K. Shapovalov, A. Iyama, T. Kimura, M. Fiebig, and D. Meier, *npj Quantum Mater.* **5**, 86 (2020).